



Experimental and numerical studies of double-nosed projectile impact on aluminum plates

M.A. Iqbal ^{a,*}, S.H. Khan ^b, R. Ansari ^b, N.K. Gupta ^c

^a Department of Civil Engineering, Indian Institute of Technology Roorkee, Roorkee, Uttarakhand 247667, India

^b Department of Mechanical Engineering, Aligarh Muslim University, Aligarh 202002, India

^c Institut für Leichtbau, RWTH Aachen University, 52062 Aachen, Germany

ARTICLE INFO

Article history:

Received 11 March 2012

Received in revised form

20 November 2012

Accepted 21 November 2012

Available online 4 December 2012

Keywords:

Double-nosed projectile

Aluminum target

Failure modes

Ballistic limit

ABSTRACT

Experiments and numerical simulations were performed to study the failure modes and ballistic resistance of aluminum targets subjected to normal impact of double-nosed projectiles. Three such projectiles used in this study were designated according to their front and second nose shapes as conico-blunt, blunt-blunt and blunt-conico. Each projectile was hit normally on 0.82 and 1.82 mm thick circular plate targets of 1100-H14 aluminium at different velocities. The deformation, failure mode and ballistic limit of both targets were obtained through experiments and reproduced through simulations using ABAQUS/Explicit finite element code. The ballistic limit of target was found to be highest against blunt-blunt followed by conico-blunt and blunt-conico projectile respectively. The results of target response thus obtained due to the impact of the double-nosed projectiles were compared with those of the single-nosed blunt and conical projectiles, and typical features of the plate response have been discussed for both double and single-nosed projectiles.

© 2012 Elsevier Ltd. All rights reserved.

1. Introduction

The nose shape of a projectile has a significant influence on the failure mode of a target. Corran et al. [1] described that an increase in the projectile nose radius changes the failure mode from ductile hole enlargement to thinning and tensile stretching to shearing of the target. Backman and Goldsmith [2] concluded that blunt missiles cause failure through plugging, wedge missiles by hole enlargement, small radius projectile by tensile stretching and sharp nosed projectile by petalling. Borvik et al. [3] mentioned that blunt nosed projectiles cause failure by shear plugging, conical projectiles through petalling in thin plates and ductile hole enlargement in thick plates while hemispherical projectiles by tensile stretching. Gupta et al. [4,5] have reported that the failure in thin ductile targets occur through shear plugging by blunt projectiles, petal formation by ogival projectile and tensile stretching by hemispherical projectile.

In addition to the failure modes, the nose shape of a projectile has also been found to have a significant effect on the ballistic limit. However, unlike the similarity of results reported in literature on the failure modes, the researchers seem to have obtained differing

results on the ballistic performance of a given projectile nose shape. Goldsmith and Finnegan [6] carried out experiments wherein cylindro-conical and blunt projectiles were impacted on 1.78 mm to 25.4 mm thick aluminum and up to 19.05 mm thick steel targets. It was observed that the nose shape of projectile has insignificant effect on the ballistic limit. Borvik et al. [3] reported that the ballistic limit of 12 mm thick Weldox 460 E steel target was 300 m/s for hemispherical and conical projectiles and 185 m/s for blunt projectile. Ipson and Recht [7] found that blunt projectiles penetrated the target more efficiently than conical projectiles when the thickness was moderate. For thin and thick targets however, an opposite trend was observed. Gupta et al. [5] concluded that ogive nosed projectile is most efficient penetrator for 0.5–1.5 mm, and blunt nosed projectile, for 2–3 mm thick aluminum targets. Iqbal et al. [8] observed that the ballistic limit of 12 mm thick Weldox 460 E steel target increased linearly with the decrease in projectile nose angle from 180° to 33.4° while Othe et al. [9] observed that the resistance of 7–38 mm thick steel targets decreased with the decrease in projectile nose angle. Corran et al. [1] reported that the perforation energy of 1.3 mm thick mild steel target increased with an increase in nose radius and reached a maximum for a critical nose radius of 11. Thereafter the perforation energy decreased sharply with further increase in the nose radius due to the transition in failure mode from shearing to tensile stretching. Iqbal et al.

* Corresponding author. Tel.: +91 1332 285866.

E-mail addresses: iqbal_ashraf@rediffmail.com, iqbalfce@iit.ernet.in (M.A. Iqbal).

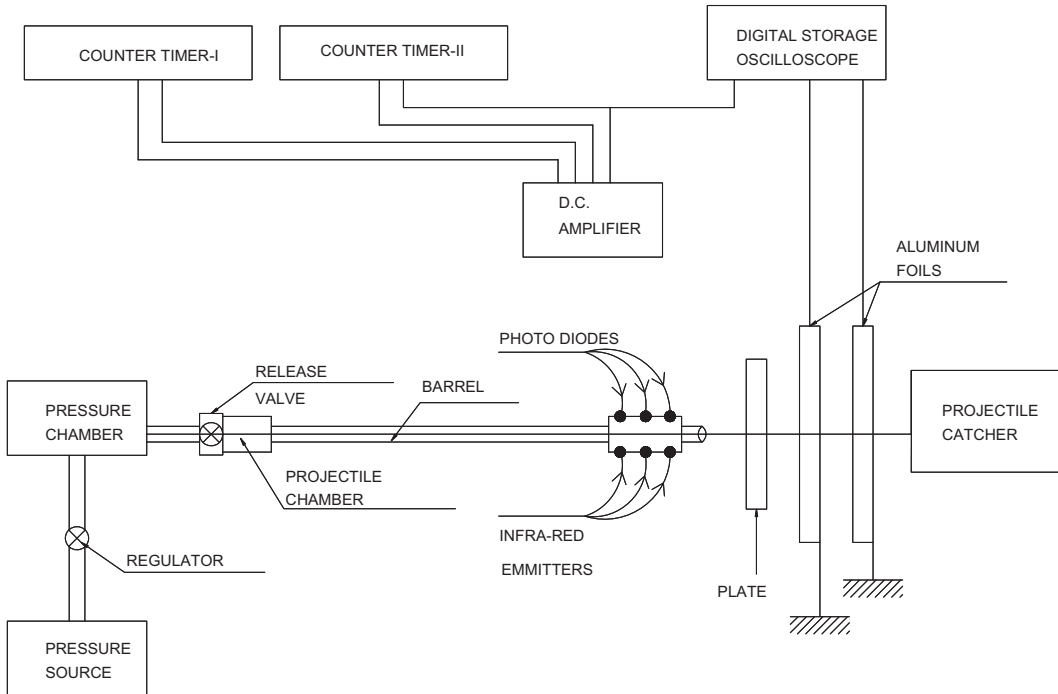


Fig. 1. Schematic of the experimental setup.

[8] observed that the ballistic limit of 1 mm thick aluminum target was not affected by changing the nose radius as long as the projectile nose shape was same. However, whenever there was transition in the nose shape (i.e., blunt, ogive, hemispherical), there was a significant effect on the ballistic limit.

The available studies are mostly restricted to a few specific nose shapes such as blunt, ogive, conical and spherical. In the present study an attempt has been made to study the effect of double-nosed stepped cylindrical projectiles (described later, see Fig. 2) on thin aluminum targets. The projectiles were designated according to their respective front and second nose shapes as conico–blunt, blunt–blunt and blunt–conico. They were made of EN-31 steel and fabricated on lathe machine to their respective shapes. The circular targets of 1100-H14 aluminum alloy with 255 mm span diameter were hit at normal incidence. The thicknesses of the targets studied were 0.82 mm and 1.82 mm. Numerical analysis was carried out using ABAQUS/Explicit finite element code [10] to predict the failure modes of the target as well as the ballistic limit. A detailed mesh convergence study was performed. The size of element was found to have an effect on the numerical results. A close correlation between the experiments and numerical simulations was found both in respect of the failure mode and the ballistic limit.

In what follows, the results of the ballistic limit, failure mode and deformation of the targets due to impact of double-nosed projectiles have been presented, discussed and compared with those of the single-nosed blunt and conical projectiles.

2. Experimental methodology

Experiments were carried out using a pneumatic gun consisting of a pressure chamber, a release valve, a projectile chamber and a barrel, Fig. 1. The impact velocity of the projectile was measured with the help of a photo gate type arrangement comprising of three infra-red light emitting diodes and three photo diodes to sense the infra-red light. For measuring the residual velocity two sets of very

thin aluminum foil screens connected to an oscilloscope were placed behind the target.

Generally the standard shapes of projectiles used by the researchers are blunt, conical, ogival and hemispherical. In this

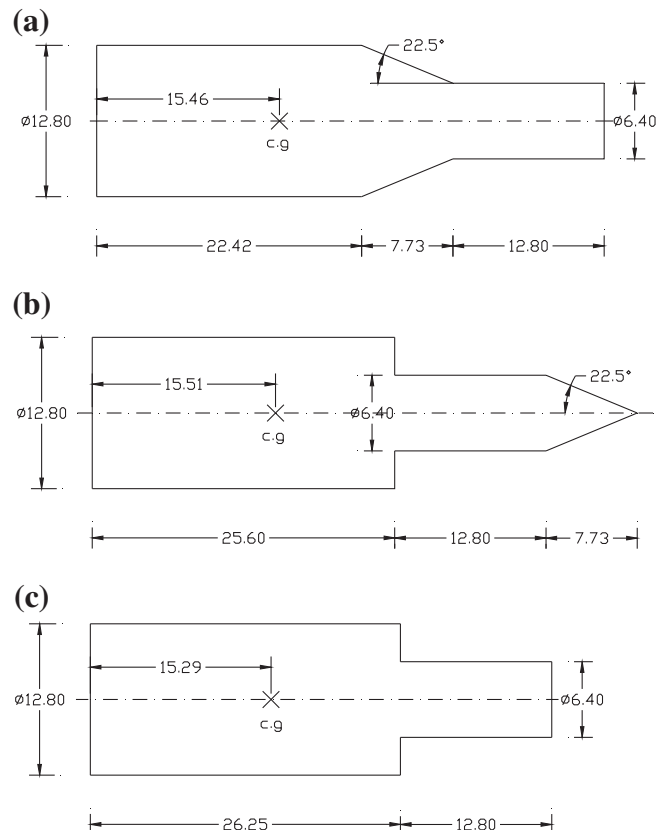


Fig. 2. Schematic of the double-nosed projectiles; (a) blunt–conico; (b) conico–blunt; (c) blunt–blunt.

study however, the effects of conical and blunt nose shapes have been combined to obtain conico–blunt, blunt–conico and blunt–blunt projectiles, see Fig. 2. The projectiles were fabricated from EN-31 steel rod by machining in a lathe machine. As shown in the figure, each projectile had two cylindrical parts with the front part diameter of 6.4 mm and the back part of 12.8 mm. Respective noses were machined in front of both parts. These machined projectiles were heated in a furnace at 920 °C for 2 h, oil quenched and tempered to 47–50 RHN. The mass of each projectile was 29.7 g and diameter in two cylindrical portions was constant. In order to keep the mass and the diameters of the three projectiles identical, the total length of the projectiles varied as 42.95, 46.13 and 39.05 mm for blunt–conico, conico–blunt and blunt–blunt projectiles respectively. The targets were circular plates of 255 mm span diameter, which were cut out of the commercially available sheets of 0.82 and 1.82 mm thicknesses of 1100-H14 aluminum alloy. The target plates were fixed to a mounting plate with the help of two mild steel rings of 8 mm thickness each. The rings were provided with eight holes of 7.9 mm diameter arranged on a 230 mm pitch circle diameter. The target plates were sandwiched between these two rings and bolted to the mounting plate. The impact velocity of the projectiles was varied between 25 m/s and 113 m/s.

3. Computational modeling

The finite element model of the projectile and target was made in the preprocessing module of the code, ABAQUS/CAE. The projectile was modeled as three-dimensional analytical rigid body with a reference point to assign mass, velocity and moment of inertia. The single-nosed projectiles were modeled with diameter (25 mm) and mass (29.7 g) equivalent to that of the larger diameter of double-nosed projectiles. The total length of the blunt projectile was 29.5 mm and that of the conical projectile 40 mm, Fig. 3. The target plate was modeled as three-dimensional deformable body. Fig. 4 shows a typical finite element model of projectile and target. The surface to surface contact between the projectile and target plate was modeled using kinematic contact algorithm with finite sliding formulation. The kinematic contact algorithm enforces constraints and conserves momentum rather too strictly. The penetration of slave nodes into the master surface is eliminated at the end of each increment. The projectile was considered as the

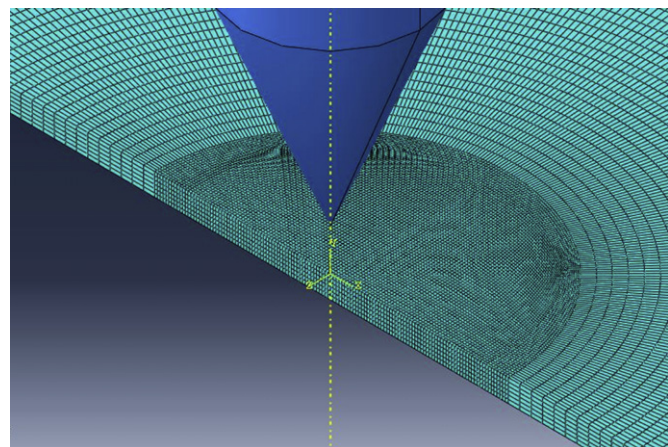


Fig. 4. Three-dimensional computational model of projectile and target.

master surface and the impact region of the plate as node based slave surface. Due to the small thickness, the friction effects between the plate and the projectile were assumed negligible. To verify this assumption, simulations were carried out at 50.8 m/s velocity with conico–blunt projectile and 0.82 mm thick target. The coefficient of friction was taken as 0 and 0.05. The residual velocity of projectile was found to be 32.21 m/s and 31.26 m/s respectively. The target plate was fixed at periphery with “encastre” boundary condition available in the code to restrict all degrees of freedom. The projectile was given an initial velocity equivalent to that obtained during experiments. For single-nosed projectiles however, the experimental results were not available therefore only the ballistic limit, defined as the average of the highest velocity giving no perforation and lowest velocity giving complete perforation of the target, was computed.

The target plates were meshed with C3D8R elements (8-node linear brick, reduced integration with hourglass control) available in the code. The reduced integration element has an advantage that the strains and stresses are calculated at locations which provide optimal accuracy. The standard numerical integration (2×2 Gaussian quadrature for a bi-linear quad, $2 \times 2 \times 2$ for a tri-linear hexa) has some problems when combined with incompressible material. The computational displacements are found to be lesser than those of their real values. This phenomenon is called volumetric locking. Theory and tests suggest that reduced integration solves this problem. Moreover, the lesser number of integration points reduces the CPU time and storage requirement. However, there is one disadvantage of reduced integration procedure that it allows the deformation mode that causes no straining at the integration point. Thus the reduced integration often causes deformation which produces no strains, hence no forces to resist. This zero-energy mode makes the element rank-deficient and results in a phenomenon called “Hourgassing”. To stabilize against this problem some artificial stiffness is provided to the element using

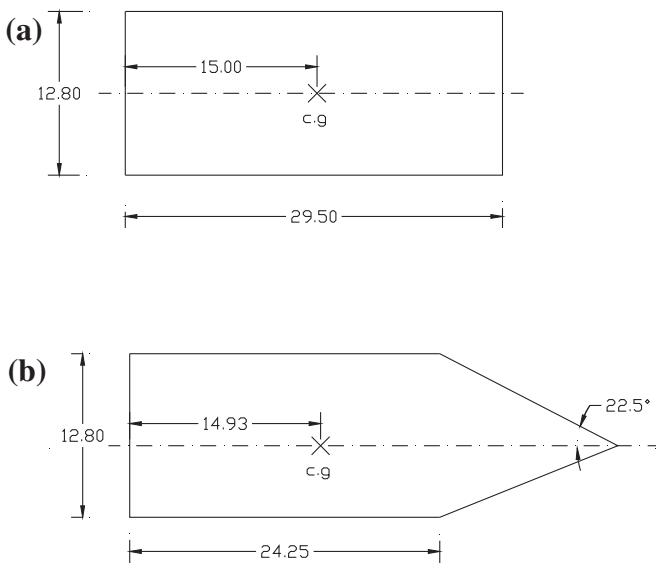


Fig. 3. Schematic of the single-nosed projectiles; (a) blunt; (b) conical.

Table 1
Variation of residual velocity with element size.

Number of elements at target thickness	Size of element (mm ³)	Residual velocity of projectile (m/s)
2	0.41 × 0.41 × 0.41	12.65
3	0.27 × 0.27 × 0.27	17.85
4	0.2 × 0.2 × 0.2	23.41
5	0.16 × 0.16 × 0.16	27.81
6	0.13 × 0.13 × 0.13	30.23
7	0.11 × 0.11 × 0.11	30.35
8	0.1 × 0.1 × 0.1	30.48

different techniques available in Abaqus/Explicit code such as enhanced, viscous, combined and relax stiffness. In the present study the analysis was carried out with each of these techniques and finally the “enhanced hourgassing” was chosen based on the optimization of results.

Meshering of the target was done to obtain accurate results within the optimum computational time. The aspect ratio of elements was maintained close to unity in the influenced region. Zukas and Scheffler [11] suggested that a numerical simulation approaches the real values when the aspect ratio approaches unity. A solution convergence study was also performed to decide the optimum size of the element. The number of elements in the case of 0.82 mm thick target was varied from 2 to 8, keeping the aspect ratio unity in the impact region. The total number of elements in the target varied as 17 248, 73 812, 134 256, 245 020, 373 996, 510 496 and 619 344 corresponding to 2–8 elements at its thickness. The target was meshed with each of the seven mesh configurations and impacted by conico-blunt projectile at a constant velocity of 50.8 m/s. This velocity was chosen being close to the ballistic limit. If the convergence is achieved at this velocity then the solution will also converge at velocities higher than this. However, the opposite may not be true [12,13]. The residual velocity of projectile, Table 1, was found to increase up to 6 elements at the thickness and thereafter it became almost constant, see Fig. 5. The number of elements was therefore considered 6 at the thickness of 0.82 mm thick target and corresponding element size $0.13 \times 0.13 \times 0.13$ mm³ for all simulations in this study. This configuration resulted in 14 elements at the thickness of 1.82 mm thick target.

4. Material modeling

The material behavior of the target, 1100-H14 aluminum was incorporated through Johnson–Cook elasto-viscoplastic material model [14,15]. It includes the effect of linear thermo-elasticity, yielding, plastic flow, isotropic strain hardening, strain rate hardening, softening due to adiabatic heating and damage. The equivalent von Mises stress $\bar{\sigma}$ of the Johnson–Cook model is expressed as

$$\bar{\sigma}\left(\dot{\varepsilon}^{\text{pl}}, \dot{\varepsilon}^{\text{pl}}, \hat{T}\right) = \left[A + B\left(\dot{\varepsilon}^{\text{pl}}\right)^n\right]\left[1 + C\ln\left(\frac{\dot{\varepsilon}^{\text{pl}}}{\dot{\varepsilon}_0}\right)\right]\left[1 - \hat{T}^m\right], \quad (1)$$

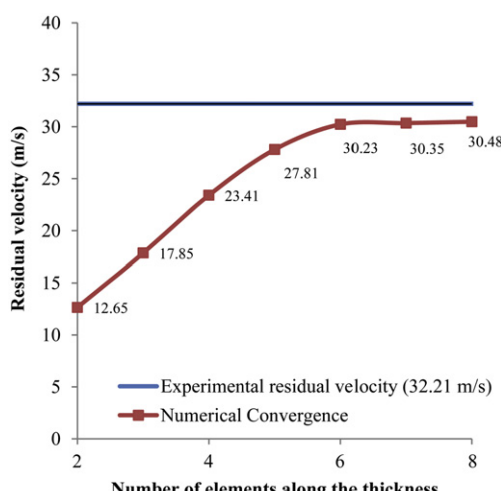


Fig. 5. Convergence of numerical results for 0.82 mm thick target hit by conico-blunt projectile.

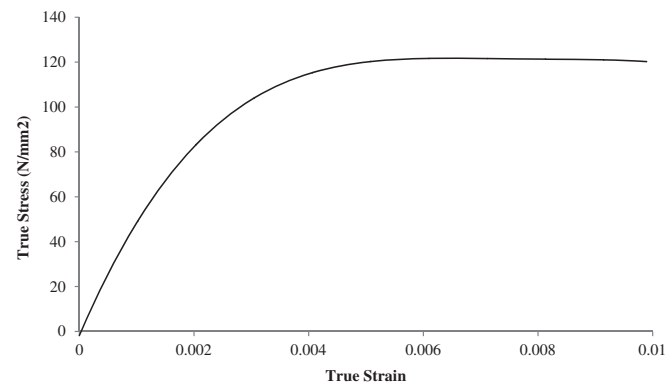


Fig. 6. True stress–strain curve for 1100-H14 aluminum alloy.

where A , B , n , C and m are material parameters. $\dot{\varepsilon}^{\text{pl}}$ is equivalent plastic strain, $\dot{\varepsilon}^{\text{pl}}$ is equivalent plastic strain rate, $\dot{\varepsilon}_0$ is a reference strain rate and \hat{T} is non-dimensional temperature defined as

$$\hat{T} = (T - T_0)/(T_{\text{melt}} - T_0) \quad T_0 \leq T \leq T_{\text{melt}} \quad (2)$$

where T is the current temperature, T_{melt} is the melting point temperature and T_0 is the room temperature. The fracture model proposed by Johnson–Cook takes into account the effect of stress triaxiality, strain rate and temperature on the equivalent fracture strain. The equivalent fracture strain $\dot{\varepsilon}_f^{\text{pl}}$ is expressed as

$$\dot{\varepsilon}_f^{\text{pl}}\left(\sigma_m, \dot{\varepsilon}, \hat{T}\right) = \left[D_1 + D_2 \exp\left(-D_3 \frac{\sigma_m}{\bar{\sigma}}\right)\right] \left[1 + D_4 \ln\left(\frac{\dot{\varepsilon}}{\dot{\varepsilon}_0}\right)\right] \left[1 + D_5 \hat{T}\right], \quad (3)$$

where D_1 – D_5 are material parameters, $\sigma_m/\bar{\sigma}$ is the stress triaxiality ratio and σ_m is the mean stress.

The material properties of 1100-H14 aluminum such as density ($\rho = 2712.6$ kg/m³), modulus of elasticity ($E = 68.948$ GPa), poison's ratio ($\nu = 0.33$) and yield stress ($A = 102.82$ MPa) were obtained from the tensile tests carried out on standard specimens prepared as per ANSI I ASTM – B557M. The true stress–strain curve thus

Table 2
Material parameters for 1100-H14 aluminum.

Modulus of Elasticity, E (N/mm ²)	68,948
Poison's Ratio, ν	0.33
Density, ρ (kg/m ³)	2712.6
Yield Stress, A (N/mm ²)	102.82
B (N/mm ²)	49.79
N	0.197
Reference Strain Rate, $\dot{\varepsilon}_0$ (s ⁻¹)	1.0
C	0.001
M	0.859
T_{melt} (K)	893
T_0 (K)	293
Specific Heat, C_p (J/kg K)	920
Inelastic heat fraction, α	0.9
Thermal conductivity, k (W/m °C)	222
D_1	0.071
D_2	1.248
D_3	-1.142
D_4	0.147
D_5	0.0
σ_{y0} for 0.82 mm thick target (N/mm ²)	104
σ_{y0} for 1.82 mm thick target (N/mm ²)	115
G_f (N/mm)	105

obtained for 1100-H14 aluminum is shown in Fig. 6. The specimens were cut from rolling and transverse directions of the sheets however, no sign of anisotropy was observed. The Johnson–Cook hardening parameters $B = 49.79$ MPa and $n = 0.197$ were taken from Ref. [16], while all the other parameters given in Table 2, including Johnson–Cook damage parameters D_1 – D_5 were assumed equivalent to those of the 1100-H12 aluminum alloy [12].

When the damage of a material occurs, the stress–strain relationship does not accurately represent its behavior. The use of true stress–strain relation during material damage introduces strong mesh dependency in the results based on strain localization such that the energy dissipated decreases as the mesh is refined. Hillerborg et al. [17] proposed the fracture energy approach to reduce mesh dependency by creating a stress-displacement response after the damage is initiated. It is defined as the energy required to open a unit crack area, G_f

$$G_f = \frac{\sigma_{y0} \times \bar{u}_f^{pl}}{2} \quad (4)$$

where σ_{y0} is ultimate stress and \bar{u}_f^{pl} is the equivalent plastic displacement at failure. With this approach the softening

response after damage initiation is characterized by a stress–displacement response rather than stress–strain response. In the present study therefore the fracture energy approach has been employed as damage evolution criterion in conjunction with Johnson–Cook damage initialization criteria. The damage evolution criterion assumes that the damage is characterized by the progressive degradation of material stiffness leading to its failure. It also takes into account the combined effect of different damage mechanisms acting simultaneously on the same material.

In order to study the influence of the damage evolution criterion on the response of the target, the residual velocities of projectiles for 0.82 mm thick target were also computed with only Johnson–Cook failure criterion, without incorporating the fracture energy approach. As such there was no significant difference between the residual velocities computed with and without fracture energy approach, Tables 3–5. However, for conico–blunt and blunt–blunt projectile the residual velocities computed without fracture energy approach showed better agreement with experimental results. On the other hand, for blunt–conico projectile, the residual velocities computed with fracture energy approach were found closer to the experiments.

Table 3

Experimental and numerical results for conico–blunt projectile.

Plate Thickness 0.82 mm														
S.No	Specimen No.	V_i (m/s)	Experimental Results				Numerical Results (JC Failure Criterion in conjunction with Fracture Energy Criterion)				Numerical Results (JC Failure Criterion)			
			V_r (m/s)	V_d (m/s)	D_{max} (mm)	No. of Petals	V_r (m/s)	V_d (m/s)	D_{max} (mm)	No. of Petals	V_r (m/s)	V_d (m/s)	D_{max} (mm)	
1	CB-A6-3	39.43	13.43	26.0	9.4	4	15.11	24.32	12.1	4	19.24	20.19	11.9	
2	CB-A5-5	50.80	32.21	18.59	9.1	5	30.23	20.57	11.7	4	33.67	17.13	11.7	
3	CB-A4-8	63.18	51.13	12.05	8.8	4	48.41	14.77	11.5	4	51.73	11.45	11.4	
4	CB-A1-9	65.56	54.11	11.45	8.8	4	52.24	13.32	11.3	4	55.17	10.39	11.3	
5	CB-A3-11	72.46	63.08	9.38	8.6	6	61.77	10.69	11.1	4	64.13	8.33	11.0	
6	CB-A2-14	86.96	79.53	7.43	8.5	4	78.14	8.82	10.0	4	79.92	7.04	10.3	
7	CB-A8-16	91.96	84.98	6.98	8.4	4	83.67	8.29	9.7	4	84.73	7.23	9.9	
8	CB-A9-19	100.0	93.81	6.19	8.2	4	92.41	7.59	8.5	4	93.22	6.78	8.5	
9	CB-A10-22	112.35	106.72	5.63	7.9	4	105.5	6.83	8.2	4	106.13	6.22	8.4	
Plate Thickness 1.82mm														
1	CB-B4-3	72.37	33.98	38.39	11.1	5	36.6	35.77	12.1	4				
2	CB-B3-5	80.64	47.33	33.31	10.9	4	49.84	30.80	11.8	4				
3	CB-B1-8	91.37	63.11	28.26	10.7	5	65.5	25.87	11.6	4				
4	CB-B2-9	100	75.22	24.78	10.3	4	77.53	22.47	11.3	4				
5	CB-B6-11	104.16	80.01	24.15	9.9	4	82.78	21.38	11.3	4				
6	CB-B7-22	113.6	91.91	21.69	9.6	4	93.44	20.16	10.9	4				

Table 4

Experimental and numerical results for blunt–blunt projectile.

S.No	Specimen No.	V_i (m/s)	Plate Thickness 0.82mm								
			Experimental Results			Numerical Results (JC Failure Criterion in conjunction with Fracture Energy Criterion)			Numerical Results (JC Failure Criterion)		
			V_r (m/s)	V_d (m/s)	D_{max} (mm)	V_r (m/s)	V_d (m/s)	D_{max} (mm)	V_r (m/s)	V_d (m/s)	D_{max} (mm)
1	BB-A4-5	55.79	38.23	17.56	10.6	37.61	18.18	9.9	39.51	16.28	10.1
2	BB-A3-8	71.4	59.62	11.78	10.3	58.10	13.30	9.6	59.45	11.95	9.7
3	BB-A2-11	86.2	77.1	9.10	10.1	75.72	10.48	9.1	76.84	9.36	9.3
4	BB-A1-14	92.59	84.98	7.61	10.0	83.35	9.24	8.8	84.34	8.25	9.0
5	BB-A6-16	100	94.1	5.90	9.7	92.35	7.64	8.6	93.1	6.9	8.8
6	BB-A7-19	103.6	97.95	5.65	9.7	96.54	7.06	8.3	97.12	6.48	8.5
7	BB-A8-21	109.3	103.69	5.61	9.5	102.85	6.44	8.0	103.22	6.08	8.2
8	BB-A8-21	113.6	108.1	5.50	9.3	107.49	6.11	7.8	107.61	5.99	8.0
Plate Thickness 1.82mm											
1	BB-B4-8	73.52	36.59	36.93	12.2	33.45	40.07	11.8			
2	BB-B3-11	80.64	57.44	23.20	11.9	54.89	25.75	11.6			
3	BB-B1-14	92.59	73.89	18.70	11.8	72.11	20.48	11.2			
4	BB-B2-16	100	82.11	17.89	11.6	80.01	19.99	11.0			
5	BB-B6-19	108.69	90.21	18.48	11.4	88.54	20.15	10.7			
6	BB-B7-22	113.6	94.49	19.11	11.3	92.15	21.45	10.5			

5. Results and discussion

Experiments and numerical simulations were carried out to study the response of 0.82 mm and 1.82 mm thick 1100-H14 aluminum target plates subjected to normal impact of double-nosed projectiles. Each projectile was impacted at different velocities in order to obtain the target profiles, incident and residual velocities, and ballistic limit. The experimental and numerical results in the form of projectile impact velocity (V_i), residual velocity (V_r), velocity drop (V_d) and maximum plate deflection (D_{max}) are given in Tables 3–5 for conico–blunt, blunt–blunt and blunt–conico projectile respectively. The number of petals formed and the maximum deformation experienced by the target have also been indicated. The specimen number mentioned in these tables indicates the projectile shape, thickness of target, number of the specimen to be experimented and the pressure of the vessel. For example CB-A6-3 indicates that the conoco–blunt projectile (CB) was impacted on 0.82 mm thick target (A) at a pressure of 3 kg/cm^2 . The impact velocity of the projectile was varied from 25 m/s to 113 m/s during the experiments, while the numerical simulations were performed with the incident velocities which were same as in corresponding experiments. For each projectile and target thickness, the velocity drop as well as the maximum target deflection was found to increase with the decrease in impact velocity. The

maximum velocity drop was found to be 38.4 m/s for conico–blunt projectile while the maximum deflection 14.9 mm for blunt–conico projectile against 1.82 mm thick target. The results also indicate a good agreement between the experimental and numerical simulation in respect of velocity drop and the maximum target damage.

The conico–blunt projectile first caused hole enlargement and petal formation due to its front conical nose, see Fig. 7(a) for experimental and (b) for numerical results, while the rear nose being blunt, failed the target through shear plugging, see Fig. 7(c–e), for numerical and (f) for experimental results. The final failure mode was actually a circular plug which ejected from the target. The plug however had a central cavity and four number of petals bent almost 90° from its surface, see Fig. 8(a) and (b) for experimental and numerical results respectively. The numerical results predicted the plug shape, which matched the experiments very well. The numerical results however predicted 4 petals at each velocity while experiments suggested that the number of petals varied from 4 to 6. The petals formed were thinner than that of the plate material. The inside circular edge of the plug was bent in the direction of projectile velocity due to the conical front nose which bent the contact region before the following blunt nose came in contact with the plate. No such bending was observed in the plug that was removed by the impact of single-nosed blunt projectile

Table 5

Experimental and numerical results for blunt-conico projectile.

S.No	Specimen No.	V_i (m/s)	Plate Thickness 0.82mm								
			Experimental Results			Numerical Results (JC Failure Criterion in conjunction with Fracture Energy Criterion)			Numerical Results (JC Failure Criterion)		
			V_r (m/s)	V_d (m/s)	D_{max} (mm)	V_r (m/s)	V_d (m/s)	D_{max} (mm)	V_r (m/s)	V_d (m/s)	D_{max} (mm)
1	BC-A4-5	54.52	44.19	10.33	12.6	46.15	8.37	11.15	49.27	5.25	11.2
2	BC-A3-8	69.44	61.95	7.49	12.6	63.57	5.87	11.1	66.21	3.23	10.9
3	BC-A2-11	83.33	76.98	6.35	12.6	78.50	4.83	11.1	80.68	2.65	10.6
4	BC-A1-14	92.41	85.78	6.63	12.5	88.34	4.07	11.0	90.11	2.3	10.7
5	BC-A6-16	100.00	93.97	6.03	12.4	95.42	4.58	10.9	96.95	3.05	10.5
6	BC-A7-19	106.60	101.51	5.09	12.4	102.76	3.84	10.8	103.94	2.66	10.4
7	BC-A8-21	109.60	104.59	5.01	12.3	105.45	4.15	10.8	106.4	3.2	10.4
Plate thickness 1.82mm											
1	BC-B4-8	73.50	52.14	21.36	14.9	54.63	18.87	13.8			
2	BC-B3-11	78.12	58.34	19.78	14.8	60.97	17.15	13.8			
3	BC-B2-14	90.15	73.21	16.94	14.8	75.54	14.61	13.7			
4	BC-B1-16	98.23	82.69	15.54	14.7	86.87	13.13	13.6			
5	BC-B6-19	103.40	87.98	15.42	14.7	90.45	12.95	13.5			
6	BC-B7-22	108.70	94.01	14.69	14.7	96.03	12.67	13.4			

and it was flat, see Fig. 9. The single-nosed conical projectile on the other hand caused failure through ductile hole enlargement and petal formation, Fig. 10. There was no sign of plug formation while the number of predicted petals was four; as in the case of the conico-blunt projectile. The petals were also found to be bent at 90° from the surface of the target. However, since the diameter of single-nosed conical projectile was double (12.8 mm) of the front part of conico-blunt projectile (6.4 mm), therefore, the size of the petals in the plates due to the impact of the former was found to be bigger than in the case of the latter.

The blunt-blunt projectile failed the target through plug formation. Two different plugs were removed from the target. The first plug was created due to the impact of the first blunt nose and the second plug by the second blunt nose of projectile, see Fig. 11(a)–(e) for numerical and (f) for experimental results. The first plug was circular and flat with diameter equal to that of the front nose. The second plug had a central hole of diameter equal to that of the front nose, while its outer diameter was equal to that of the projectile. Single-nosed blunt projectile however, caused ejection of a single plug whose diameter was same as that of the blunt nose. The numerical simulations revealed that the velocities with which the first plug that was ejected by the blunt-blunt projectile and the plug that was ejected by the single-nosed blunt projectile were higher than that of the respective projectiles. It may be due to the fact that impact of these blunt noses of the projectiles imparted

an impulse to the indented area of the respective plates, causing the ejected plugs with relatively small masses to accelerate. However, no such acceleration was noticed in the case of the second plug ejected by the double-nosed projectile, which remained attached to the projectile after ejection. The same was also observed in the experiments wherein the second plug was found stuck with the recovered projectile. Fig. 12(a) and (b) shows typical experimental and computed plugs respectively, ejected from 0.82 mm thick plate impacted by blunt-blunt projectile.

The blunt-conico projectile ejected the first plug of diameter equal to its blunt nose with speed higher than that of the projectile, see Fig. 13(a) and (b) for numerical results. Thereafter the conical portion expanded the hole created by the blunt part and bulged it in forward direction, see Fig. 13(c) and (d) for numerical results. However, the petal formation could not be seen in this case in contrast to that of the failure caused by its opposite nose combination, conico-blunt. This is due to the fact that the growth of petals occurs by the pointed tip of the projectile which first creates a star shaped crack in the target material and thereafter the hole enlargement causes the formation of petals, see Figs. 7 and 10. In this case however, due to the absence of conical tip the formation of petals could not be seen. The bulged region of the target was thinner due to the stretching of material by the conical portion of the projectile, see Fig. 13(e) and (f) for experimental and numerical results respectively. The thickness of the bulge was found to be

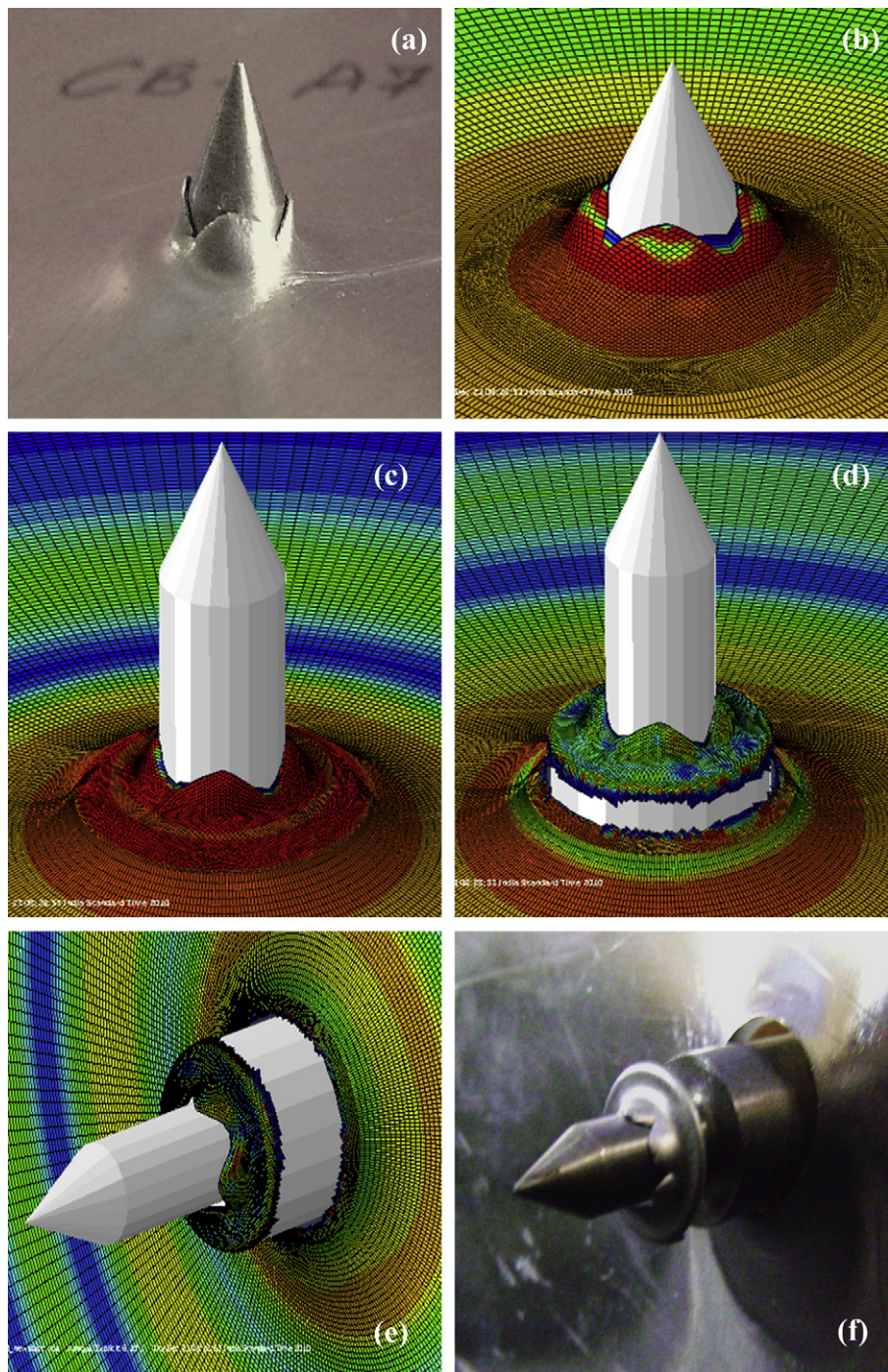


Fig. 7. Failure of 0.82 mm thick target by conico–blunt projectile.

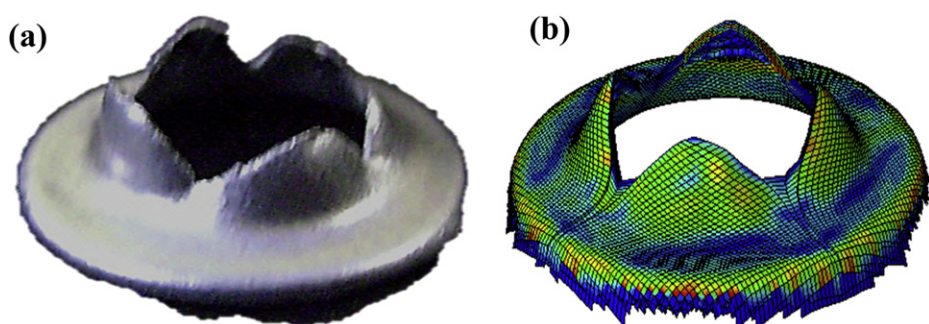


Fig. 8. Plug removed from 0.82 mm thick target impacted by conico–blunt projectile; (a) experimental and (b) numerical results.

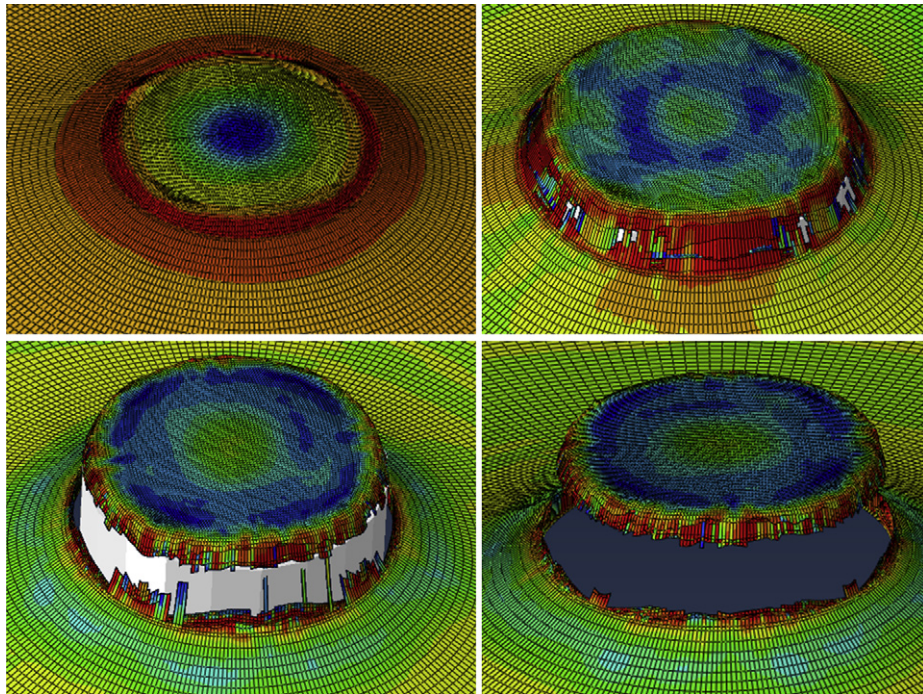


Fig. 9. Failure of 1.82 mm thick target by single-nosed blunt projectile.

0.59 mm from experiments, Fig. 14(a), and 0.55 mm from the numerical results, Fig. 14(b), for 0.82 mm thick target.

Fig. 15(a) shows the actual and predicted deformation profiles of 0.82 and 1.82 mm thick targets impacted by conico-blunt

projectile. In a few experiments and numerical simulations performed for impact by this projectile, some fragmentations of the target material were observed after the formation of petals just above the ballistic limit velocity. The bending was small and

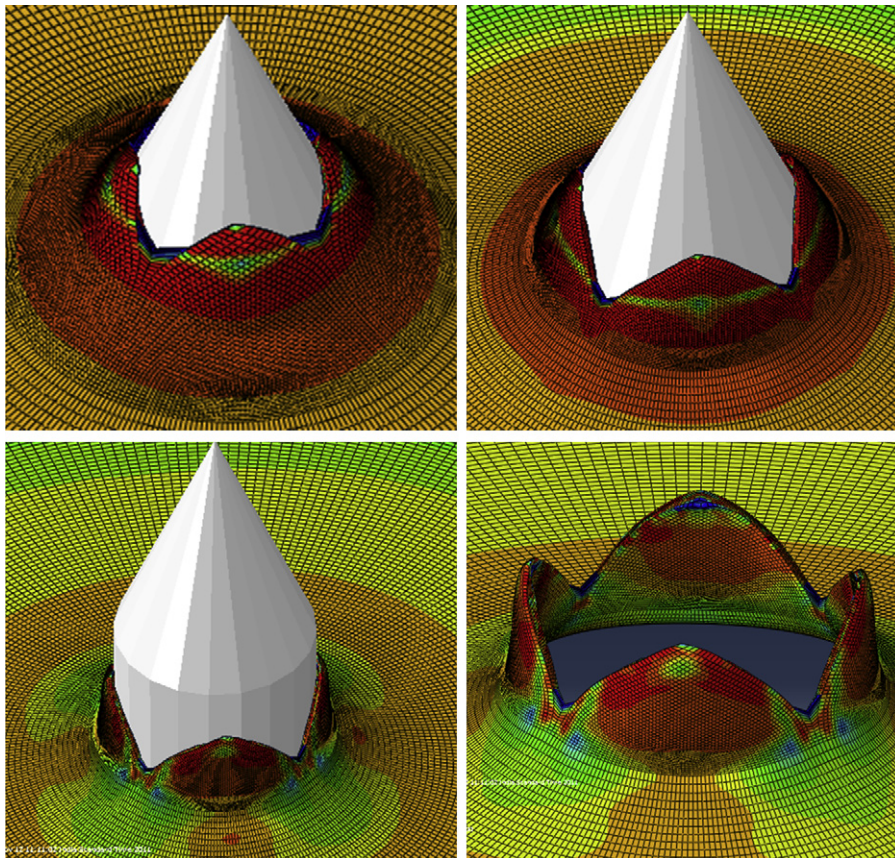


Fig. 10. Failure of 1.82 mm thick target by single-nosed conical projectile.

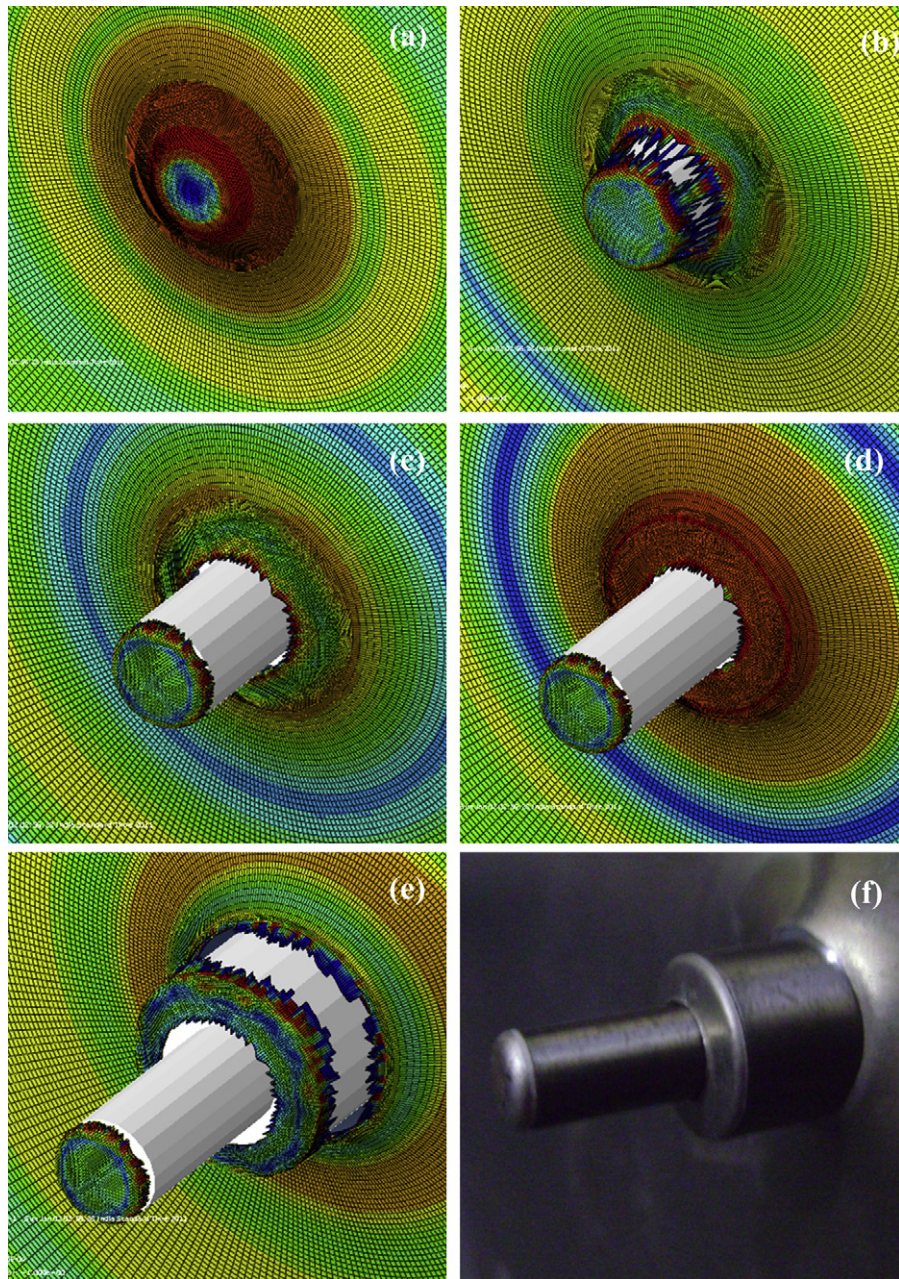


Fig. 11. Failure of 0.82 mm thick target by blunt–blunt projectile.

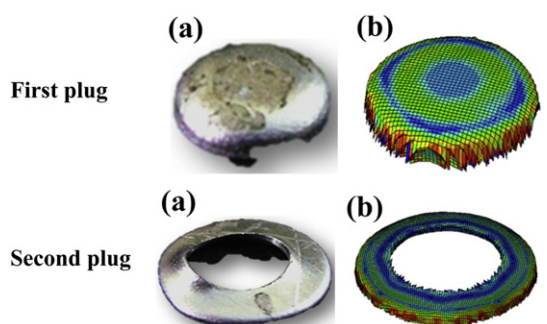


Fig. 12. Plugs removed from 0.82 mm thick target impacted by blunt–blunt projectile; (a) experimental and (b) numerical results.

localized initially when conical nose perforated the target. However, its magnitude and span increased when the blunt nose came in contact and finally it spread over the entire span of the target. The deformation profile is plotted at 39.43 m/s velocity for 0.82 mm and 72.37 m/s for 1.82 mm thick targets. For blunt–blunt projectile the deformation was localized and higher in intensity as compared to the other two double-nosed projectiles, Fig. 15(b). Thinning of the target material was absent in this case and thickness of both plugs was found equal to that of the impacted plate. The deformation was plotted at 55.7 m/s velocity for 0.82 mm and at 73.5 m/s velocity for 1.82 mm thick targets. The dishing in both target thicknesses was found close to each other. The deformation of target was also found to be more localized for blunt–conico projectile, Fig. 15(c). Thinning of the deformed region was also noticed. However, the global

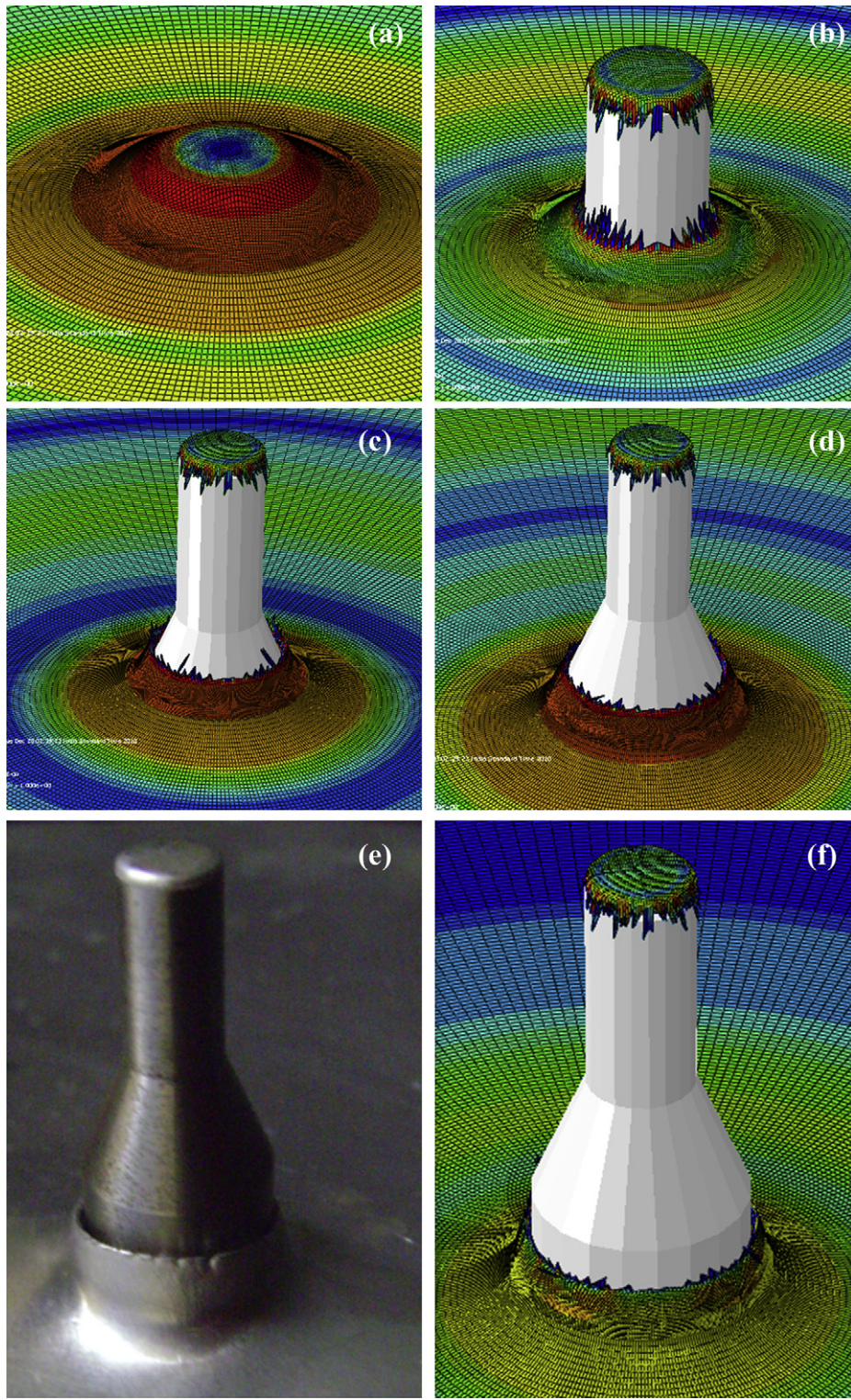


Fig. 13. Failure of 0.82 mm thick target by blunt-conico projectile.

deformation was found lowest in this case due to the hole enlargement. The deformation in this case was plotted at 54.5 m/s velocity for 0.82 mm and 73.5 m/s velocity for 1.82 mm thick targets. For each projectile and target thickness, the numerically obtained deformation profile was found to match the experimental profile well, though slightly over predicted. In general, the deformation was found to increase with an increase in target

thickness and decrease in impact velocity. At the periphery of the target the magnitude of deformation in both thicknesses was almost same. However, near the impact zone it became more apparent in thicker target.

The residual velocity curves of conico-blunt, blunt-blunt and blunt-conico projectiles are shown in Fig. 16(a)–(c) respectively. As such the actual and predicted residual velocities matched very

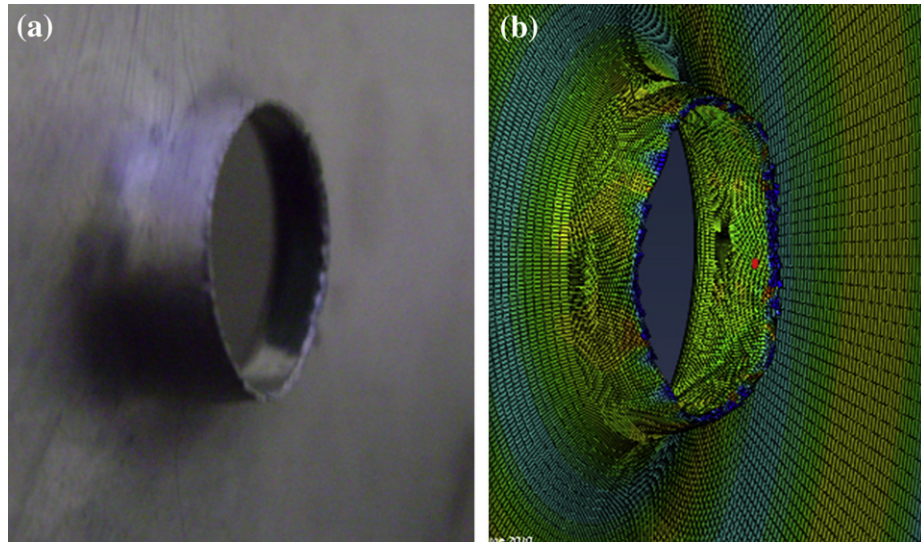


Fig. 14. Bulging of 0.82 mm thick target by conical nose of the blunt-conico projectile; (a) experimental; and (b) numerical results.

well for each of the three double-nosed projectiles. The computations with the finite element code gave the ballistic limit within 8% of the experimental values, Table 6. The initial projectile velocities giving no perforation and complete perforation of the target,

employed to calculate the predicted value of the ballistic limit are also shown in Table 6. The values of both of these initial velocities have been carefully acquired in order to correctly predict the ballistic limit.

In general the ballistic limit of 1.82 mm thick target was found almost double to that of the 0.82 mm thick target. The actual ballistic limit for 1.82 mm thick target was found to be 94%, 82% and 135% higher than 0.82 mm thick target for conico-blunt, blunt-blunt and blunt-conico projectile respectively. The same was predicted to be 101.3%, 72.4%, 147.6%, 100.3% and 93.8% respectively for conico-blunt, blunt-blunt, blunt-conico, single-nosed conical and single-nosed blunt projectile. It may therefore be concluded that the blunt-conico projectile has given a highest ballistic limit difference between the two thicknesses.

It was also observed that 0.82 mm thick target offered highest ballistic limit against blunt-blunt projectile followed by single-nosed blunt projectile. On the other hand, 1.82 mm thick target offered highest ballistic limit against single-nosed blunt projectile followed by blunt-blunt projectile. The failure mechanism of single-nosed blunt projectile and blunt-blunt projectile was identical to each other except the fact that the later has caused the failure of target in two stages due to its double nose shape. The single-nosed blunt projectile caused highest global deformation of 1.82 mm thick target while the blunt-blunt projectile caused highest global deformation of 0.82 mm thick target, see Fig. 17. It was also noticed that 0.82 mm thick target offered lowest ballistic limit against blunt-conico projectile followed by single-nosed conical projectile, while 1.82 mm thick target offered lowest ballistic limit against single-nosed conical projectile followed by blunt-conico projectile. The mode of deformation was petalling by single-nosed conical projectile, plugging was caused by the front nose of the blunt-conico projectile, and only hole enlargement by its second nose.

For double-nosed projectiles however, the actual as well as predicted ballistic limit values of both target thicknesses were found to be highest against blunt-blunt projectile followed by conico-blunt and blunt-conico projectile respectively.

To further investigate the influence of the projectile nose shape the predicted velocity drop and energy absorbed due to the first and second nose of the double-nosed projectile was separately

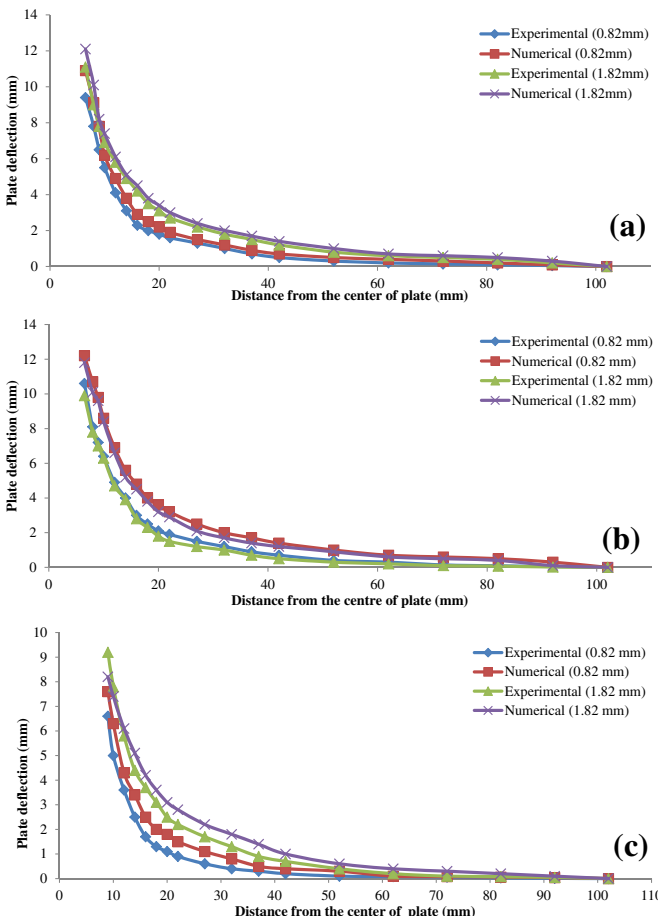


Fig. 15. Global dishing of 0.82 mm and 1.82 mm thick target by (a) conico-blunt; (b) blunt-blunt and (c) blunt-conico projectile.

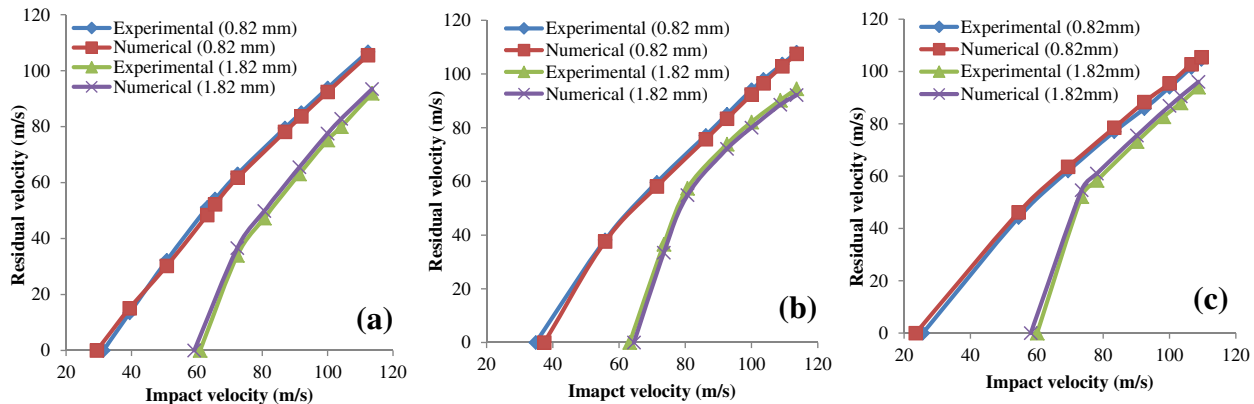


Fig. 16. Actual and predicted residual velocity curves for (a) conico-blunt; (b) blunt-blunt and (c) blunt-conico projectile.

Table 6

Actual and predicted ballistic limit velocities for 0.82 mm and 1.82 mm thick targets.

Projectile shape	Target thickness			
	Experimental results (m/s)		Numerical results (m/s)	
	0.82 mm	1.82 mm	0.82 mm	1.82 mm
Conico-blunt	31.4	60.9	(29 + 29.8)/2 = 29.4	(57.4 + 61)/2 = 59.2
Blunt-blunt	34.8	63.2	(36.6 + 38.2)/2 = 37.4	(62 + 67)/2 = 64.5
Blunt-conico	25.6	60.1	(22.5 + 24.5)/2 = 23.5	(57.1 + 59.3)/2 = 58.2
Conical	—	—	(26 + 28.2)/2 = 27.1	(53 + 55.6)/2 = 54.3
Blunt	—	—	(33.5 + 35.1)/2 = 34.3	(64.8 + 68.2)/2 = 66.5

evaluated for 0.82 mm thick target at 100 m/s velocity, please see Table 7. The absorbed energy for the individual nose was then compared with the similar nose of other double-nosed as well as single-nosed projectiles. The second nose of the conico-blunt projectile has been found to dissipate maximum energy ($E_2 = 0.55$ J; $V_{d2} = 6.1$ m/s) followed by the single-nosed blunt projectile ($E_1 = 0.423$ J; $V_{d1} = 5.38$ m/s) and second nose of the blunt-blunt projectile ($E_2 = 0.38$ J; $V_{d2} = 5.1$ m/s) respectively. The energy dissipated by the first nose of the blunt-conico and blunt-blunt projectiles was found identical. The single-nose conical projectile was found to dissipate higher energy ($E_1 = 0.243$ J; $V_{d1} = 4.05$ m/s) compared to the second nose of the blunt-conico projectile ($E_2 = 0.061$ J; $V_{d2} = 2.02$ m/s).

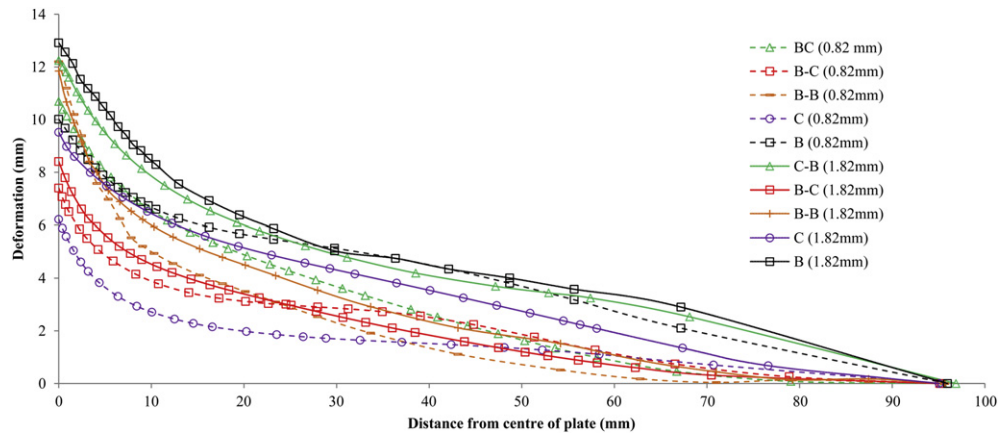


Fig. 17. Predicted global target deformation for single as well as double-nosed projectiles (B-B: blunt-blunt; B-C: blunt-conico; C-B: conico-blunt; B: single-nosed blunt; C: single-nosed conical).

Table 7

Energy absorbed by target due to individual nose of the projectile.

Projectile	Impact by first nose			Impact by second nose		
	V_{d1} (m/s)	E_1 (J)	Fracture mechanism	V_{d2} (m/s)	E_2 (J)	Fracture mechanism
Conico-blunt	1.43	0.030	Petaling/Stretching	6.1	0.55	Plugging/Shearing
Blunt-blunt	2.59	0.099	Plugging/Shearing	5.1	0.38	Plugging/Shearing/fragmentation
Blunt-conico	2.56	0.097	Plugging/Shearing	2.02	0.061	Bulging/Stretching
Conical	4.05	0.243	Petaling/Stretching	—	—	—
Blunt	5.38	0.423	Plugging/Shearing	—	—	—

V_{d1}, V_{d2} : Velocity drop by the first and second nose; E_1, E_2 : Energy absorbed by the first and second nose.

It has also been observed from Table 7 that the blunt nose required more perforation energy than that of the equivalent diameter conical nose.

6. Conclusions

Experimental and numerical studies were conducted wherein the ballistic resistance of 0.82 and 1.82 mm thick 1100-H14 aluminum targets was studied against the normal impact of double-nosed projectiles. Computed and experimental values of residual velocities as well as ballistic limit matched very well for each of the three double-nosed projectiles.

The failure mechanism of the plates when impacted by the blunt–blunt projectile was the ejection of two plugs due to successive impacts of front and second blunt noses. Thus two plugs formed successively. The single-nose projectile results in only one plug. The conico–blunt projectile removed a plug from the target, which had a central cavity and four number of petals bent almost 90° from its surface. The circular edge of this plug was bent in the direction of projectile velocity in contrast to that of the flat plug caused by the single-nosed blunt projectile. The single-nosed conical projectile also caused failure through petal formation and the number of computed petals was four, as was in the case of the conico–blunt projectile. The blunt–conico projectile ejected a plug of diameter equal to its blunt nose and then the rear portion caused bulging of the hole created by the front nose. However, the petal formation could not be seen in this case as was seen in the case of its opposite nose combination, viz., conico–blunt.

For 0.82 mm thick target the ballistic limit was found to be highest against blunt–blunt projectile followed by single-nosed blunt, conico–blunt, single-nosed conical and single-nosed blunt projectile respectively. For 1.82 mm thick target the ballistic limit was found to be highest against single-nosed blunt projectile followed by blunt–blunt, conico–blunt, blunt–conico and single-nosed conical projectile respectively.

It has also been observed that for a given diameter the projectile with blunt nose required more perforation energy than that of the conical nose.

Acknowledgment

Prof. Gupta would like to thank DFG, Germany, and Prof. H G Reimerdes for supporting his stay at RWTH Aachen University as Mercator Guest Professor.

References

- [1] Corran RSJ, Shadbolt PJ, Ruiz C. Impact loading of plates – an experimental investigation. *Int J Impact Eng* 1983;1:3–22.
- [2] Backman ME, Goldsmith W. The mechanics of penetration of projectiles into targets. *Int J Eng Sci* 1978;16:1–99.
- [3] Borvik T, Langseth M, Hopperstad OS, Malo KA. Perforation of 12 mm thick steel plates by 20 mm diameter projectiles with flat, hemispherical and conical noses. Part I. Experimental study. *Int J Impact Eng* 2002;27:19–35.
- [4] Gupta NK, Iqbal MA, Sekhon GS. Effect of projectile nose shape, impact velocity and target thickness on the deformation behavior of layered plates. *Int J Impact Eng* 2008;35:37–60.
- [5] Gupta NK, Iqbal MA, Sekhon GS. Effect of projectile nose shape, impact velocity and target thickness on deformation behavior of aluminum plates. *Int J Solid Struct* 2007;44:3411–39.
- [6] Goldsmith W, Finnegan SA. Normal and oblique impact of cylindro-conical and cylindrical projectiles on metallic plates. *Int J Impact Eng* 1986;4:83–105.
- [7] Ipsos TW, Recht RF. Ballistic perforation by fragments of arbitrary shape. NWC TP 5927. China Lake, CA, USA: Denver Research Institute, Naval Weapons Centre; 1977.
- [8] Iqbal MA, Gupta G, Diwakar A, Gupta NK. Effect of projectile nose shape on the ballistic resistance of ductile targets. *Eur J Mech A Solid* 2010;29:683–94.
- [9] Othe S, Yoshizawa H, Chiba N, Shida S. Impact strength of steel plates struck by projectiles. *Bull JSME* 1982;25:1226–31.
- [10] ABAQUS analysis user's manual, Version 6.10.1, vol. 2. Providence, Rhode Island, USA: Dassault Systemes Simulia Corporation; 2010.
- [11] Zukas JA, Scheffler DR. Practical aspects of numerical simulations of dynamic events: effects of meshing. *Int J Impact Eng* 2000;9:925–45.
- [12] Gupta NK, Iqbal MA, Sekhon GS. Experimental and numerical studies on the behavior of thin aluminum plates subjected to impact by blunt- and hemispherical-nosed projectiles. *Int J Impact Eng* 2006;32:1921–44.
- [13] Iqbal MA, Chakrabarti A, Beniwal S, Gupta NK. 3D numerical simulations of sharp nosed projectile impact on ductile targets. *Int J Impact Eng* 2010;37:185–95.
- [14] Johnson GR, Cook WH. A constitutive model and data for metals subjected to large strains, high strain rates and high temperatures. In: Proceedings of the seventh International symposium on Ballistics. Washington DC, USA: American Defense Preparedness Association; 1983. p. 541–7.
- [15] Johnson GR, Cook WH. Fracture characteristics of three metals subjected to various strains, strain rates, temperatures and pressures. *Eng Fract Mech* 1985;21:31–48.
- [16] <http://www.varmintal.com/aengr.htm>.
- [17] Hillerborg A, Modeer M, Petersson PE. Analysis of crack formation and crack growth in concrete by means of fracture mechanics and finite elements. *Cement Concr Res* 1976;6:773–82.